




Copper plating on water-soluble NaCl particles by evaporative crystallization and its effect on the pore structure of infiltrated AlSi12 alloy foam

Qianfu Xia¹, Xiaoqing Zuo^{1,*} , Yun Zhou¹, Jianhong Yi¹, and Bei Huang¹

¹ Faculty of Material Science and Engineering, Kunming University of Science & Technology, Kunming 650093, Yunnan, People's Republic of China

Received: 7 February 2023

Accepted: 8 May 2023

Published online:
29 May 2023

© The Author(s), under exclusive licence to Springer Science+Business Media, LLC, part of Springer Nature 2023

ABSTRACT

A new evaporative crystallization method was used to plate copper on water-soluble NaCl particles. $\text{Cu}(\text{NO}_3)_2 \cdot 3\text{H}_2\text{O}$ was crystallized on NaCl particles by the heated ethanol volatilization, and then thermally decomposed to obtain CuO coating which was finally reduced to Cu coating. The affecting factors of coating effect and the influence of copper-plated NaCl particles on the pores structure of infiltrated AlSi12 foam were studied. The thermal oxidation pretreatment of NaCl particles increased the number of oxygen-containing functional groups and the uniform distribution of thermal etch pits, which improved the bonding strength between NaCl particles and $\text{Cu}(\text{NO}_3)_2 \cdot 3\text{H}_2\text{O}$ coating. The addition of Tween-60 and PEG-6000 inhibited the micro-dissolution of NaCl particles in ethanol and promoted the formation of complete CuO coating. Infiltrated AlSi12 foam prepared from copper-plated NaCl particles had a more homogeneous pore structure and smaller pore size deviations than infiltrated AlSi12 foam obtained with uncoated NaCl particles, indicating that copper plating significantly improved the wettability of NaCl particles and AlSi12 alloy melt. This paper presents a new and low-cost surface treatment method, which provides a useful reference for the surface modification and application of water-soluble particles.

Introduction

Open-cell aluminum foam has a large number of through holes with complex structure, which has the strong sound absorption ability in a wide frequency

range [1–3]. It has important application prospects in noise control fields such as transportation, construction and machinery [4, 5]. In particular, small apertures of 300–500 μm greatly increase the resistance to incident sound waves and provide better sound

Handling Editor: Catalin Croitoru.

Address correspondence to E-mail: zxqdzhhm@kmust.edu.cn

absorption than large apertures of 500 μm and above. Infiltration is the mainstream method for preparing open-cell aluminum foam, which has the advantages of simple process and easy mass production [6, 7]. The surface properties of the preformed NaCl particles directly influences the pore structure of the open-cell aluminum foam [8]. The infiltration preparation of large-aperture open-cell aluminum foam has been achieved [9]. However, when the pore size of open-cell aluminum foam prepared by infiltration is decreasing, greater pressure is required to make the molten aluminum infiltrate into the gap of the NaCl particle preform. As a result, it is highly susceptible to problems such as insufficient depth of infiltration and incomplete infiltration [10], the reasons for which are related to the wettability of the NaCl particles and the aluminum melt.

The surface treatment of NaCl particles is an effective method to improve the wettability between aluminum melt and NaCl particles, but there are few reports on its research. Electroless plating [11–14] and electroplating [15–17] are common surface metalization processes, in which Ni and Cu are commonly used for surface treatment of nonmetallic particles. However, in the process of electroless plating and electroplating, the matrix particles will contact with deionized water [12, 18, 19], so these methods are not applicable to the surface modification of water-soluble NaCl particles. Magnetron sputtering as a physical vapor deposition technique is widely used in the formation of various surface coatings [20]. Tučkutė et al. deposited nickel on the surface of NaCl particles by magnetron sputtering and then cleaned the Ni-coated NaCl particles in water to obtain Ni powder with a flaky structure [21], but this method was not suitable for mass production. Therefore, the use of a new low-cost surface treatment for the coating of NaCl particles is an important development direction to improve the performance of infiltration preparation processes for open-cell aluminum foam materials, especially for small pore size open-cell aluminum foam.

For that reason, this paper used a novel EC method for copper plating on NaCl particles. The affecting factors of the coating effect and the influence of copper-plated NaCl particles on the pores structure of infiltrated AlSi12 foam were investigated. Copper plating on water-soluble NaCl particles provides a beneficial reference for the stable infiltration

preparation of small pore size sound-absorbing aluminum foam.

Experimental

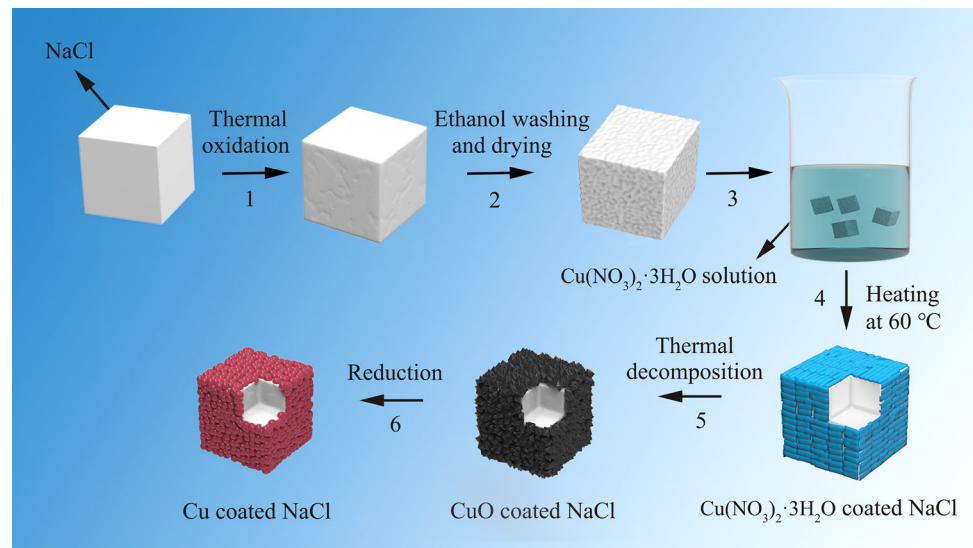
Materials

Polygonal sodium chloride particles with a particle size of 270–300 μm (NaCl, Yunnan Salt Industry Co., Ltd.) were used as plating substrate. Copper nitrate trihydrate ($\text{Cu}(\text{NO}_3)_2 \cdot 3\text{H}_2\text{O}$, Fuchen Chemical Reagent Co., Ltd.) as the copper source. Anhydrous ethanol ($\text{C}_2\text{H}_6\text{O}$, Fuchen Chemical Reagent Co., Ltd.) as the solvent. Tween-60 ($\text{C}_{64}\text{H}_{126}\text{O}_{26}$, Wuxi Yatai Joint Chemical Co., Ltd.) as the stabilizer. PEG-6000 ($\text{HO}(\text{CH}_2\text{CH}_2\text{O})_{\text{nH}}$, Wuxi Yatai Joint Chemical Co., Ltd.) as the surfactant. 95% Argon (Ar) and 5% hydrogen (H_2) (Kunming Shitouren Gas Product Co., Ltd.) as the reduction gas and AlSi12 as the infiltration alloy.

EC copper plating process

Figure 1 shows the schematic diagram of the EC copper plating process on NaCl particles, which consists of six steps. Step 1, the pretreatment of NaCl particles was carried out by thermal oxidation method. The NaCl particles were placed in a muffle furnace and treated at 400 $^\circ\text{C}$ for 40 min with a heating rate of 10 $^\circ\text{C}/\text{min}$, following by cooling down to room temperature naturally outside the furnace. Step 2, the thermally oxidized NaCl particles were placed in anhydrous ethanol, where the ethanol:NaCl ratio was 2:3, ultrasonically washed for 10 min to remove impurities, then dried in a blast drying oven. Step 3, the $\text{Cu}(\text{NO}_3)_2 \cdot 3\text{H}_2\text{O}$ solution was prepared with anhydrous ethanol, $\text{Cu}(\text{NO}_3)_2 \cdot 3\text{H}_2\text{O}$ (135 g/L), Tween-60 (10 g/L), PEG-6000 (1 g/L) and the pretreated NaCl particles (1500 g/L). Step 4, the $\text{Cu}(\text{NO}_3)_2 \cdot 3\text{H}_2\text{O}$ solution with NaCl particles was continuously heated in a water bath at 60 $^\circ\text{C}$, stirring while heating until the anhydrous ethanol was completely volatilized. Step 5, the NaCl particles were placed in a muffle furnace and treated at 340 $^\circ\text{C}$ for 2 h with a heating rate is about 3 $^\circ\text{C}/\text{min}$, following by cooling down to room temperature naturally outside the furnace. Step 6, hydrogen reduction, the NaCl particles were placed in a tube furnace with a continuous flow of hydrogen at 1L/min, and treated

Figure 1 Schematic diagram of the EC copper plating on NaCl particles.



at 500 °C for 2 h with a heating rate is about 10 °C/min, following by cooling down to room temperature naturally within the furnace.

AlSi12 alloy melt infiltration

Copper-plated NaCl particles were prepared according to a mass ratio of 1/5 between $\text{Cu}(\text{NO}_3)_2 \cdot 3\text{H}_2\text{O}$ to NaCl particles. Under the condition of the same quality of uncoated copper and copper-coated NaCl preforms, the AlSi12 alloy melt was subjected to air pressure infiltration of 0.10–0.30 MPa at a heating temperature of 680 °C. Finally, the copper-coated and uncoated NaCl/AlSi12 composites were immersed in water to remove NaCl particles.

Characterization

Morphology, element

The morphology of NaCl particles, coatings and infiltrated AlSi12 foam pore structure were observed by scanning electron microscope (SEM, Nova-Nano450/ZEISS). The oxygen-containing functional groups of NaCl particles surface at the pretreatment stage were detected by Fourier transform infrared spectroscopy (FT-IR, Tensor27). The phase analysis of the coatings at different stages was carried out by X-ray diffractometer (XRD, Empyrean) which the radiation source is CuK α , the working voltage is 20 kV, the working current is 40 mA, the scanning speed is 6°/min, the time constant of the rate

recorder is 0.5 s, and the diffraction angle range is 10–90°. The obtained data were calibrated and analyzed by jade6.0 software to determine the phase composition.

Porosity

The porosity of the infiltrated AlSi12 alloy foam was calculated by the following equation.

$$\phi = 1 - \frac{\rho_{Al}}{\rho_0} \cdot 100\% = 1 - \frac{M}{V} \cdot \frac{1}{\rho_0} \cdot 100\% \quad (1)$$

where ϕ is the porosity of the infiltrated AlSi12 foam, ρ_0 is the density of the substrate material, ρ_{Al} is the density of the infiltrated AlSi12 foam, M is the mass of the infiltrated AlSi12 foam, and V is the volume of the infiltrated AlSi12 foam.

Desalination rate

The desalination rate of the infiltrated AlSi12 alloy foam was calculated by the following equation.

$$X = \frac{M_0 - M_1}{M} \cdot 100\% \quad (2)$$

where X is the desalination rate, M_0 is the total mass of the AlSi12/NaCl composite, M_1 is the mass of the AlSi12/NaCl composite after removal of the NaCl, and M is the mass of the NaCl preform.

Coating rate

The coating rate was calculated by the following equation.

$$\eta = \frac{S_D}{S} \cdot 100\% \quad (3)$$

η is the coating rate, S_D is the coated area of the NaCl particle surface, and S is the area of the NaCl particles surface. S_D , S were obtained by ImageJ image processing software.

Results and discussion

Effect of NaCl particle pretreatment on the $\text{Cu}(\text{NO}_3)_2 \cdot 3\text{H}_2\text{O}$ coating

Figure 2 shows SEM images of NaCl particles at different pretreatment stages. As can be seen from Fig. 2a, b, the surface of untreated NaCl particles is relatively flat and smooth, its brightness is caused by the nonconductivity of NaCl. As shown in Fig. 2c, d that the surface of NaCl particles has obvious pits at the thermal oxidation stage. The reason is that NaCl particles are heated in the muffle furnace for a period of time, thermal etch pits are formed at the intersection of grain boundary and surface in order to achieve the balance of surface tension [22–24]. It can be seen from Fig. 2e, f, the thermal etch pits are evenly distributed on the NaCl particles at the washing and drying stage. The formation of thermal pits can cause an ‘anchoring effect’ between the $\text{Cu}(\text{NO}_3)_2 \cdot 3\text{H}_2\text{O}$ coating and NaCl particles, improving the bond strength [25–28] and laying the foundation for a homogeneous and stable copper coating.

Figure 3 shows the Fourier transform infrared spectra of NaCl particles at different pretreatment stages. As can be seen from Fig. 3, the absorption peak at 617 cm^{-1} is attributed to the -OH swaying vibration, the absorption peak at 1113 cm^{-1} is caused by the C–O–C stretching vibration, the absorption peak at 1643 cm^{-1} is attributed to the C=O stretching vibration, and the absorption peak at 3442 cm^{-1} is caused by the -OH stretching vibration [29, 30]. The absorption peak at 1422 cm^{-1} is caused by the -OH bending vibration at the thermal oxidation stage. At the washing and drying stage, the peaks of the thermal oxidation stage are retained. It can be seen from Fig. 3 that the oxygen-containing functional groups

on the surface of NaCl particles after thermal oxidation increase, that is, the surface of NaCl particles fixes a large amount of oxygen in the form of functional groups, which increases the wettability of the surface of NaCl particles and enhances the bonding strength of NaCl particles and $\text{Cu}(\text{NO}_3)_2 \cdot 3\text{H}_2\text{O}$.

Figure 4 is the SEM image of the untreated and pretreated NaCl particles after copper plating. It can be seen from Fig. 4a and b that the surface of NaCl particles without pretreatment is relatively smooth, and copper particles are scattered on the NaCl particles. As can be seen from Fig. 4c and d, the surface of NaCl particles after pretreatment is rough, and copper particles are distributed more in the rough position, while copper particles are scattered in the flat surface. Compared with the copper-plated NaCl particles without pretreatment, the copper coating area of NaCl particles obtained after pretreatment increased. The results show that the adhesion of copper particles is stronger where the surface of NaCl particles is rough.

Effect of Tween-60 and PEG-6000 on the CuO coating

Figure 5 represents SEM images of NaCl particles at different stages. It can be seen from Fig. 5a, without the addition of Tween-60 and PEG-6000, rectangular crystals with a width of about $1.5 \mu\text{m}$ are densely arranged on the NaCl particles at the evaporative crystallization stage. Figure 6 shows the XRD pattern of NaCl particles at different stages. As seen from Fig. 6, without the addition of Tween-60 and PEG-6000, the only two phases with significant peak heights are NaCl and $\text{CuCl}_2 \cdot 2\text{H}_2\text{O}$ at the evaporative crystallization stage. Therefore, it is determined that the rectangular crystals obtained without the addition of Tween-60 and PEG-6000 are $\text{CuCl}_2 \cdot 2\text{H}_2\text{O}$. The appearance of $\text{CuCl}_2 \cdot 2\text{H}_2\text{O}$ indicates that NaCl particles are slightly dissolved in ethanol, and free chloride ions are combined with copper ions. With the volatilization of anhydrous ethanol, $\text{CuCl}_2 \cdot 2\text{H}_2\text{O}$ is crystallized on the NaCl particles. As shown in Fig. 5b, at the thermal decomposition stage without Tween-60 and PEG-6000, flake crystals were distributed on the surface of NaCl particles, and the coating rate was 47.5%. Figure 6 shows that when Tween-60 and PEG-6000 are not added, only NaCl and CuO phases have obvious peak heights at the thermal decomposition stage, so it is determined that

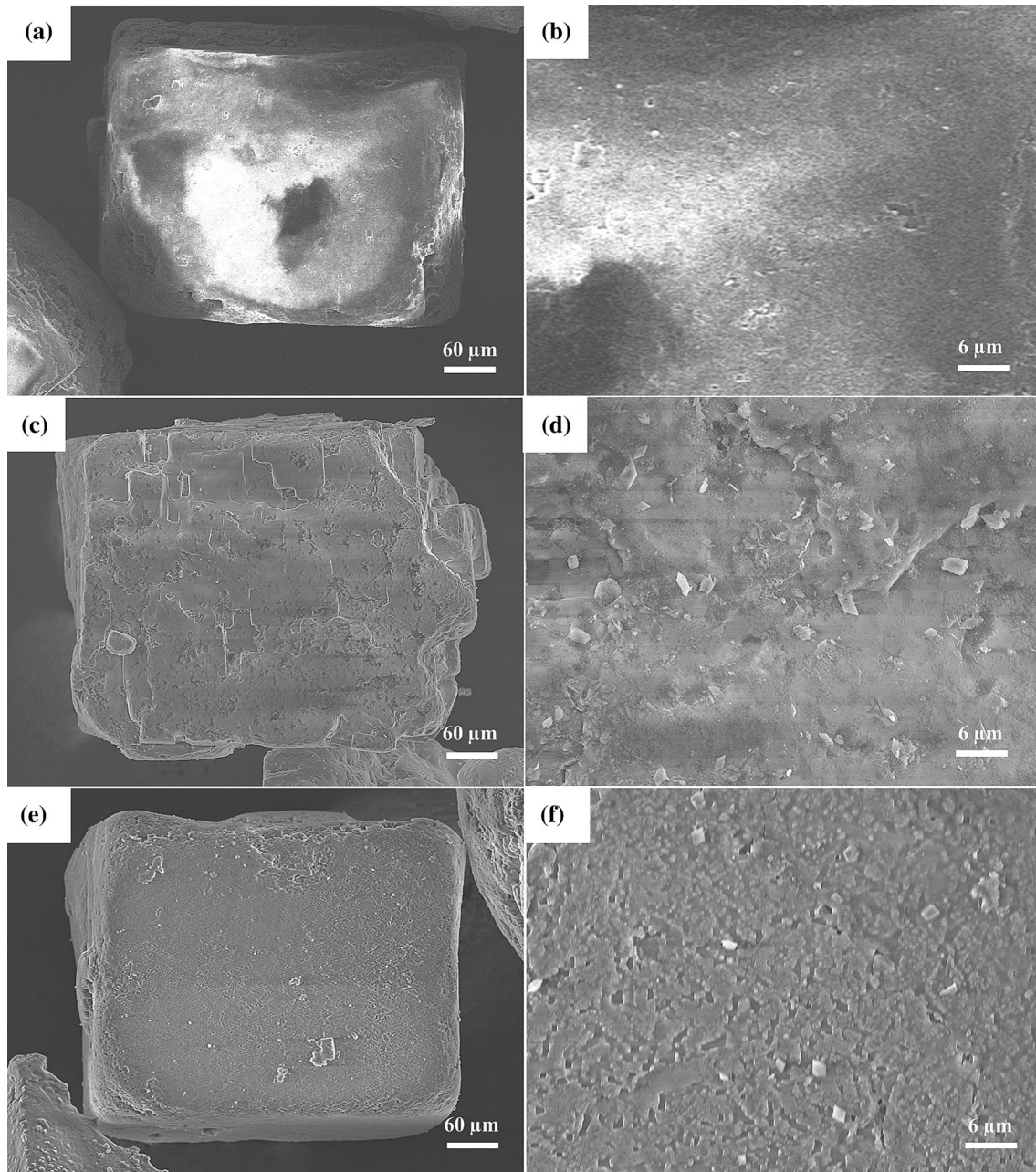


Figure 2 SEM images of NaCl particles at different pretreatment stages: **a, b** untreated, **c, d** thermal oxidation, **e, f** washing and drying.

the flake crystals formed in the thermal decomposition stage are CuO.

As seen in Fig. 5c, when only Tween-60 is added, rectangular crystals with a width of 2–8 μm are densely arranged on the NaCl particles at the evaporative crystallization stage. It can be seen from Fig. 6, when only Tween-60 is added, the two phases with significant peak heights are NaCl and $\text{Cu}(\text{NO}_3)_2 \cdot 3\text{H}_2\text{O}$ at the evaporative crystallization stage. Therefore, it is determined that the rectangular

crystals formed at the evaporative crystallization are $\text{Cu}(\text{NO}_3)_2 \cdot 3\text{H}_2\text{O}$, indicating that the addition of Tween-60 inhibits the micro-dissolution of NaCl particles in ethanol. As can be seen from Fig. 5d, When Tween-60 was added only, granular crystals were distributed on the surface of NaCl particles at the thermal decomposition stage, and the coating rate was 90.47%. Compared with the coating area of CuO without Tween-60, the coating area is significantly increased, but the NaCl particles are still not fully

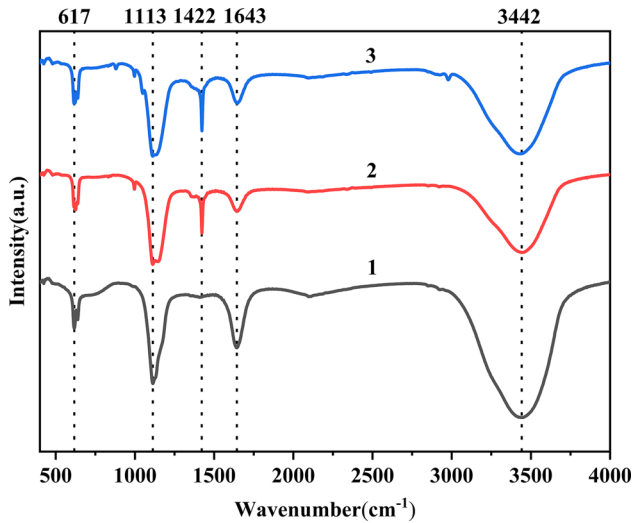


Figure 3 Fourier transform infrared spectra of NaCl particles at different pretreatment stages: 1-Untreated, 2-Thermal oxidation and 3-Washing and drying.

coated. Figure 6 shows that when only Tween-60 is added, the only two phases with significant peak heights are NaCl and CuO at the thermal

decomposition stage, so it is determined that the granular crystals formed at the thermal decomposition are CuO. After the addition of Tween-60, the coating area of CuO on the NaCl particles increases significantly. It is speculated that the addition of Tween-60 decreases the interfacial tension and decline the total interfacial energy, thus achieving a significant increase in the coating area. Besides, Tween-60 has the property of decreasing the surface tension of the solution, which can diminish the contact angle between solid and liquid and decline the capillary adsorption force between NaCl particles [31], thus effectively avoids the phenomenon of NaCl particle agglomeration.

It can be seen from Fig. 5e that with the addition of Tween-60 and PEG-6000, the rectangular crystals with a width of 2–8 μm are densely arranged on the NaCl particles at the evaporative crystallization stage. Figure 6 shows that when Tween-60 and PEG-6000 are added, only two phases NaCl and $\text{Cu}(\text{NO}_3)_2 \cdot 3\text{H}_2\text{O}$ have obvious peak heights at the evaporative crystallization stage, and the only two

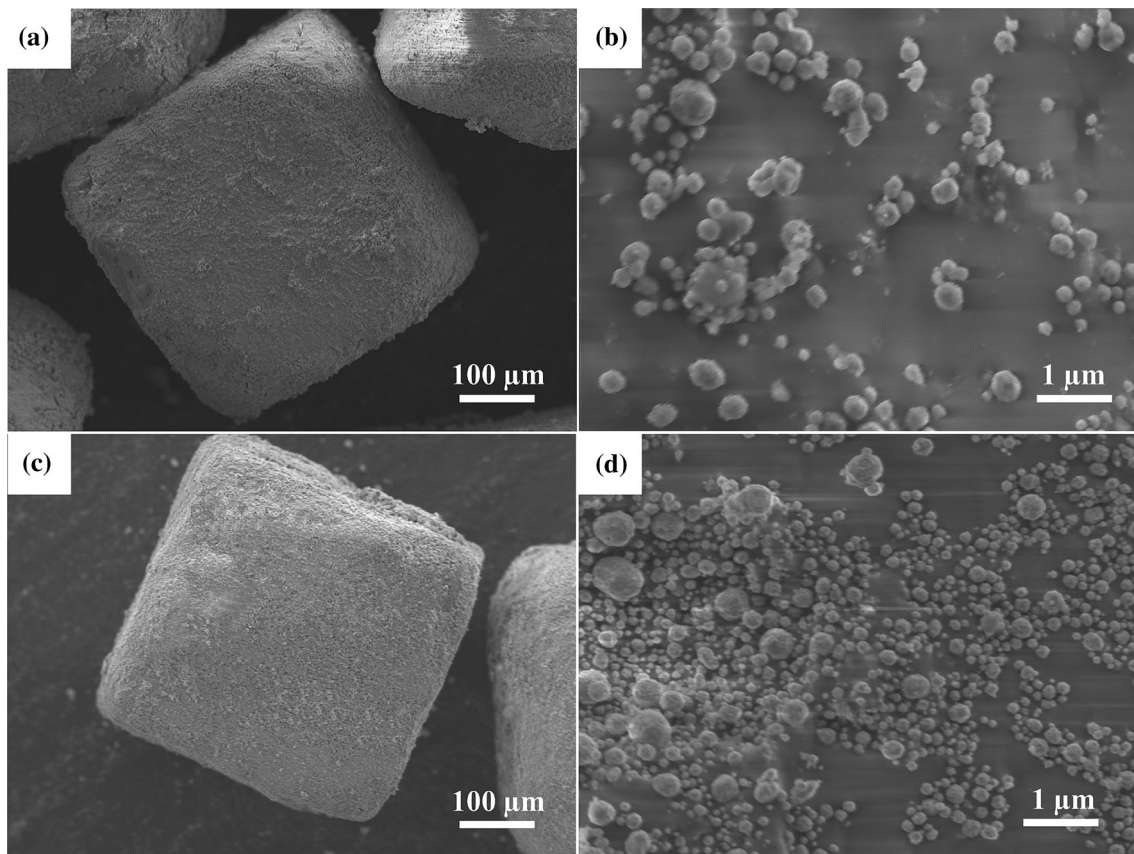


Figure 4 SEM images of copper-plated NaCl particles: **a, b** untreated NaCl particles, **c, d** pretreated NaCl particles.

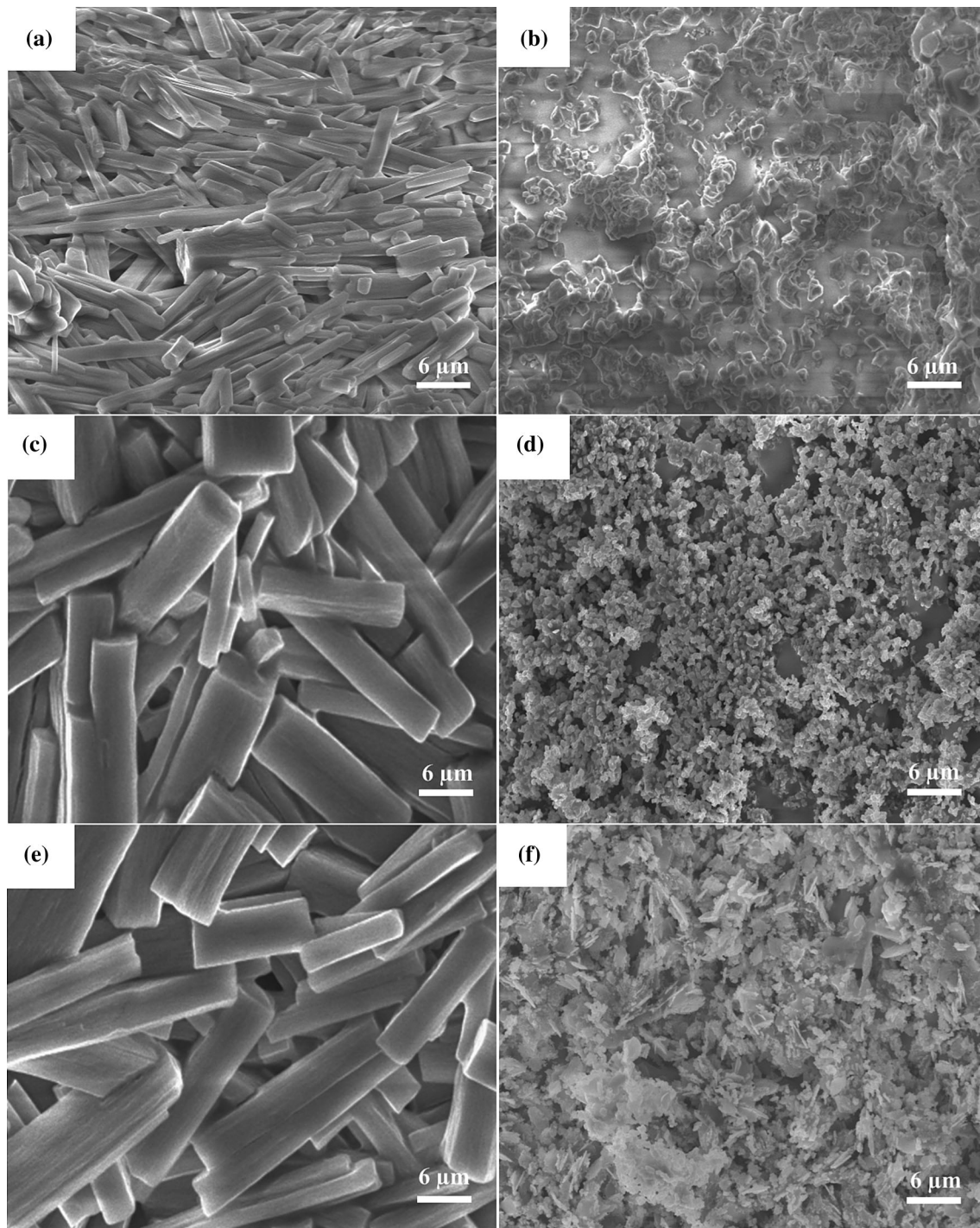


Figure 5 SEM images of NaCl particles at different stages: **a** evaporative crystallization, without Tween-60 and PEG-6000, **b** thermal decomposition, without Tween-60 and PEG-6000, **c** evaporative crystallization, only Tween-60, **d** thermal

decomposition, only Tween-60, **e** evaporative crystallization, with Tween-60 and PEG-6000 and **f** thermal decomposition, with Tween-60 and PEG-6000.

phases with significant peak heights are NaCl and CuO at the thermal decomposition stage. Therefore, the crystals formed at the evaporative crystallization

stage are $\text{Cu}(\text{NO}_3)_2 \cdot 3\text{H}_2\text{O}$, and the crystals formed at the thermal decomposition stage are CuO. As can be seen from Fig. 5f, NaCl particles can be almost

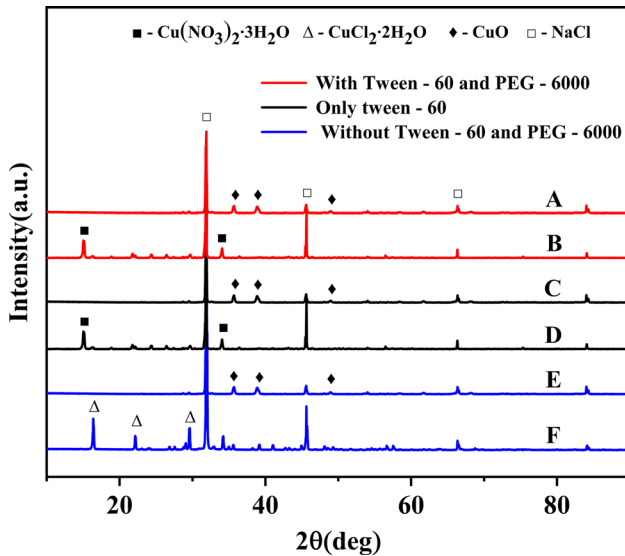


Figure 6 XRD patterns of NaCl particles at different stages: Evaporative crystallization—B, D, F, Thermal decomposition—A, C, E.

completely coated by CuO when Tween-60 and PEG-6000 are added at the thermal decomposition stage. The addition of PEG-6000 changes the crystal morphology of CuO, indicating that PEG-6000 has an important effect on the growth direction of CuO crystals [32]. During the thermal decomposition to generate CuO, flatness of the plating is affected by the escape of the gas, resulting in the loss of CuO plating. The addition of PEG-6000 with a suitable amount can wet the coating and make the generated gas easily remove from the coating.

In summary, the addition of Tween-60 and PEG-6000 inhibits the micro solubilization of NaCl particles in ethanol and substantially increases the CuO coating area on NaCl particles.

Formation process of the Cu coating

Figure 7 shows SEM images of NaCl particles at different stages. It can be seen from Fig. 7a, b that the rectangular crystals are densely arranged on the NaCl particles at the evaporative crystallization stage. Figure 8 represents the XRD pattern of NaCl particles at different stages. It can be seen from Fig. 8, the two phases with significant peak heights are NaCl and $\text{Cu}(\text{NO}_3)_2 \cdot 3\text{H}_2\text{O}$ at the evaporative crystallization stage, so it is determined that the rectangular crystals are $\text{Cu}(\text{NO}_3)_2 \cdot 3\text{H}_2\text{O}$.

As seen in Fig. 7c, d, the NaCl particles are densely coated at the thermal decomposition stage. Figure 8 represents the only two phases with significant peak heights are NaCl and CuO at the thermal decomposition stage. It is determined that the coating formed on the NaCl particles at the thermal decomposition phase is CuO. The transformation of the coating from $\text{Cu}(\text{NO}_3)_2 \cdot 3\text{H}_2\text{O}$ to CuO is shown in Fig. 9 [33].

Figure 7(e, f) represents the granular crystals are densely distributed on the NaCl particles at the reduction stage. As shown in Fig. 8, the strong diffraction peaks are located at 43.3° (corresponding to the Cu(111) plane), 50.4° (corresponding to the Cu(200) plane) and 74.1° (corresponding to the Cu(220) plane) at the reduction stage [27, 34]. Therefore, it is determined that the granular crystal is Cu, and no CuO, Cu_2O and other phases are found.

Figure 10 shows the crystal structure of CuO and Cu. During the reduction of CuO, H adsorbs on the surface of CuO, and O in CuO of monoclinic system is taken away by H to form Cu with face-centered cubic structure [35]. The reduction of CuO to Cu results in a 42.3% increase in volume contraction so that decreases lattice size and decline surface coverage. Therefore, the premise for achieving complete Cu coating is to realize a multilayer dense CuO coating of the NaCl particles.

Effect of copper-plated NaCl particles on the pore structure of infiltrated AlSi12 alloy foam

Under the condition of the same mass of uncoated and copper-coated NaCl preforms, AlSi12 alloy melt was infiltrated in the uncoated NaCl preform at 0.25 MPa pressure for 6 s, and aluminum foam with porosity of 86% was obtained. AlSi12 alloy melt was infiltrated in the copper-coated NaCl preform at 0.15 MPa pressure for 3 s, and aluminum foam with porosity of 83% was obtained. Compared to the infiltration of AlSi12 alloy melt in the uncoated NaCl preform, the gas pressure applied to complete the infiltration in the copper-coated NaCl preform is decreased and the holding time is shortened. This indicates copper plating significantly improves the wettability of NaCl particles and AlSi12 alloy melt, which has a noticeable improvement in the fluidity of AlSi12 alloy melt in the copper-plated NaCl preform.

Figure 11 shows the SEM images of the infiltrated AlSi12 alloy foam. As can be seen from Fig. 11a,

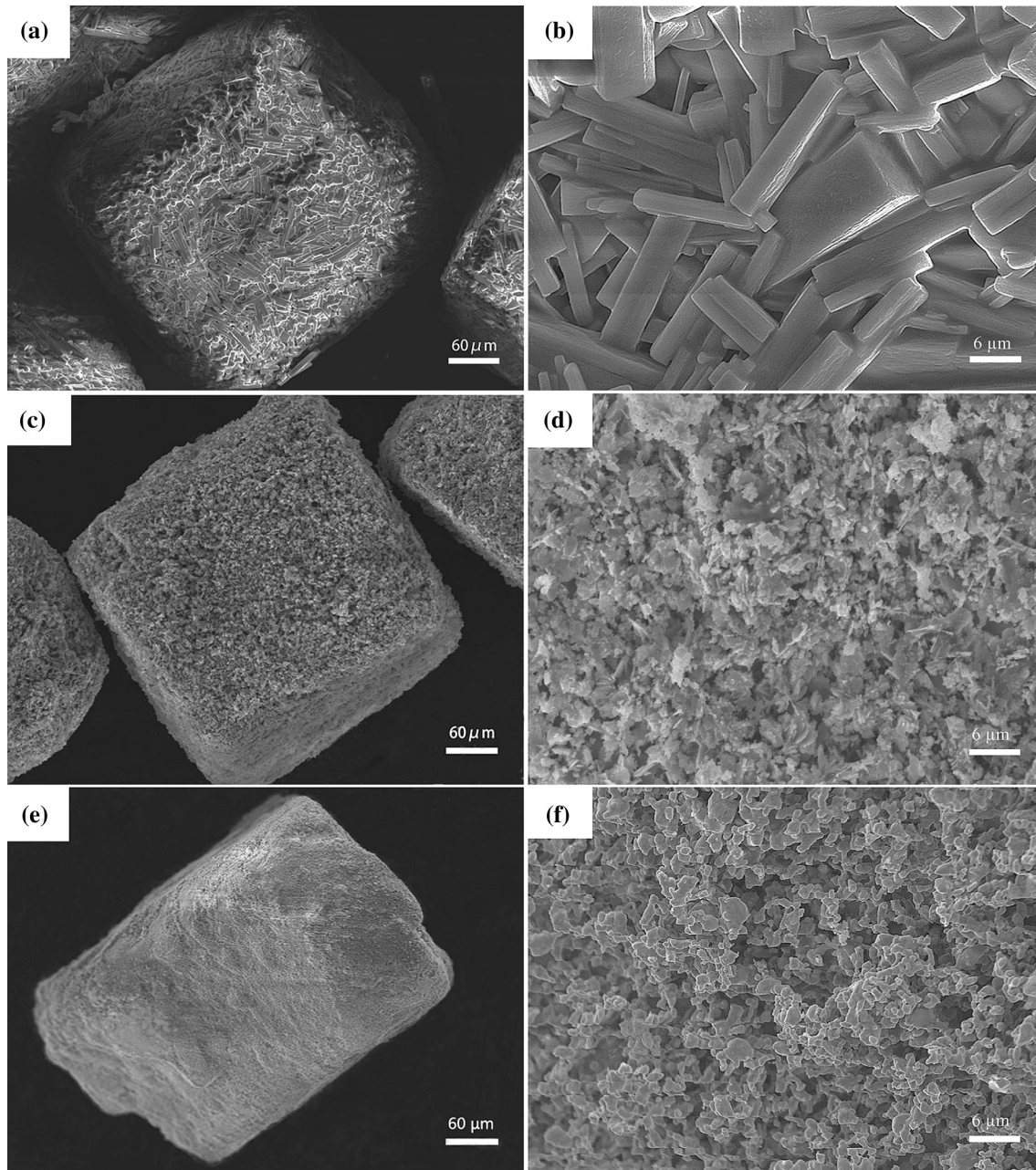


Figure 7 SEM images of NaCl particles at different stages: **a, b** evaporative crystallization, **c, d** thermal decomposition, **e, f** reduction.

when the uncoated NaCl particles are used as preform, the pores of the AlSi12 alloy foam are connected to each other, and the AlSi12 alloy is interlaced in the form of a frame. However, it is shown that the pore shape is irregular, the pore size range is large, and the pore walls of some pores are incomplete. It can be seen from Fig. 11b that the pore structure of the infiltrated AlSi12 alloy foam is

relatively uniform when using copper-plated NaCl particles as the preform. Most of the pores are square, the pore wall is relatively complete, and the adjacent pores are connected with each other. Almost no obvious defects and closed pore structure can be seen.

The pore sizes in Fig. 11 were obtained by ImageJ and the following results were obtained by numerical

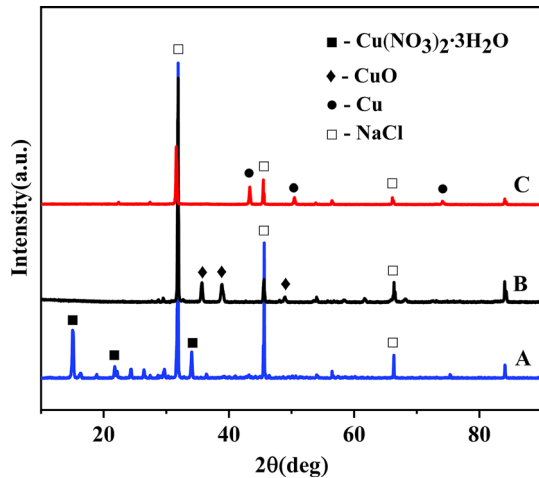


Figure 8 XRD patterns of NaCl particles at different stages: A-Evaporative crystallization, B-Thermal decomposition and C-Reduction.

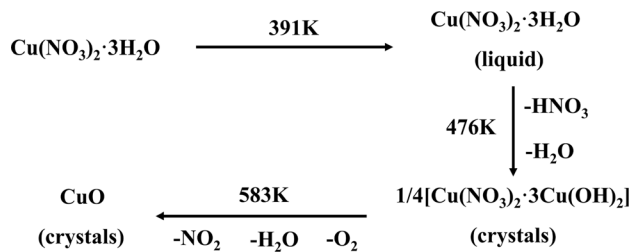


Figure 9 Thermal decomposition process of copper nitrate trihydrate to copper oxide.

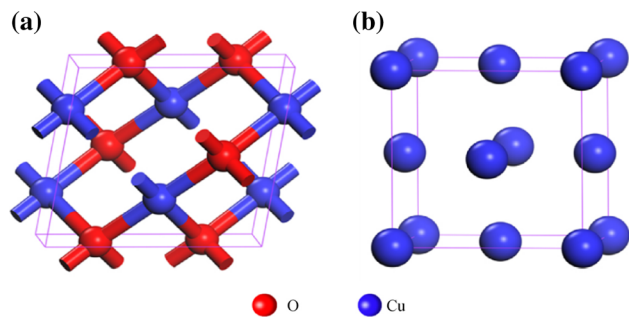


Figure 10 The crystal structure of a CuO and b Cu.

calculation. The average pore size of aluminum foam prepared from uncoated NaCl particles was 302 μm, with a pore size deviation of 67.55 μm. The average pore size of the aluminum foam prepared from copper-coated NaCl particles was 238 μm, with a pore size deviation of 52.77 μm. Compared with aluminum foam prepared by uncoated NaCl particles, the pore size deviation of aluminum foam prepared

by copper-coated NaCl particles is smaller. The results show that the wettability between the copper-plated NaCl particles and the AlSi12 alloy melt is improved, and the contact between the both is more adequate during the infiltration process. Additionally, according to the calculation of formula (3), the salt removal rate of the infiltrated AlSi12 foam is 95%.

Analysis of wettability in infiltration process

Figure 12 presents a schematic diagram to illustrate the infiltration process of AlSi12 alloy melt to NaCl particles with the different surface states. As seen from this figure, the gravity of the AlSi12 alloy melt is $\rho_{\text{AlSi12}}gh$, the capillary pressure difference is ΔP , θ is the wetting angle. The capillary pressure difference of AlSi12 alloy melt during infiltration can be obtained by Laplace–Young equation [36]:

$$\Delta P = \frac{2\gamma \cos\theta}{r_c} \tag{4}$$

where ΔP is the capillary pressure difference, γ is the surface tension of the AlSi12 alloy melt, θ is the wetting angle between NaCl particles and AlSi12 alloy melt and r_c is the equivalent capillary radius.

It can be seen from formula (4), for the wetting angle of NaCl particles and AlSi12 alloy melt, when $\theta < 90^\circ$, $\Delta P > 0$, ΔP promotes the passage of AlSi12 melt. When $\theta > 90^\circ$, $\Delta P < 0$, ΔP hinders the passage of AlSi12 melt.

The wetting angle between Al melt and NaCl particles is more than 150° at 800°C . Figure 12a shows the infiltration process of AlSi12 alloy melt to the uncoated NaCl particles. It can be seen from the figure, wetting angle $\theta > 150^\circ$ between AlSi12 alloy melt and NaCl particles, so they are difficultly wetted [37]. Figure 12b shows the infiltration process of AlSi12 alloy melt to NaCl particles which is coated with copper particles. AlSi12 droplet is nonspherical due to gravity. The relationship between h and θ can be expressed by the following formula [38]:

$$h = \left\{ 2 \left(\frac{\gamma}{\rho g} \right) [1 - \cos(\theta + \alpha)] \right\}^{1/2} \left[1 + \left(\frac{\gamma}{\rho g} \right)^{1/2} \frac{2}{2a} \right]^{-1/2} \tag{5}$$

where h is the height between the horizontal line of the liquid–gas–solid intersection and the endpoint of the long axis of the droplet ($h = 1 \text{ mm}$), γ is the surface tension of AlSi12 melt ($\gamma = 871.82 \text{ mN/m}$), ρ is the

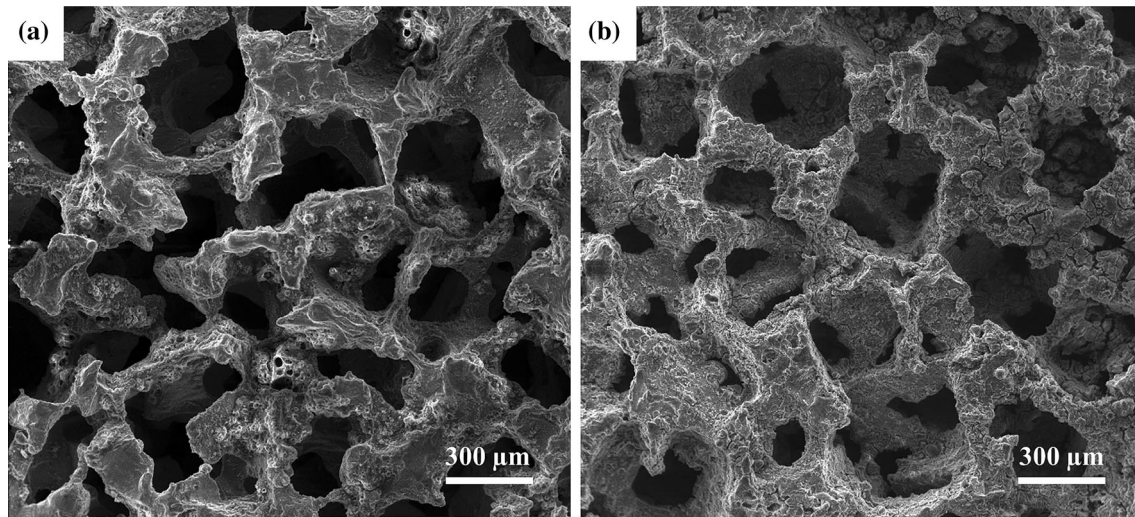
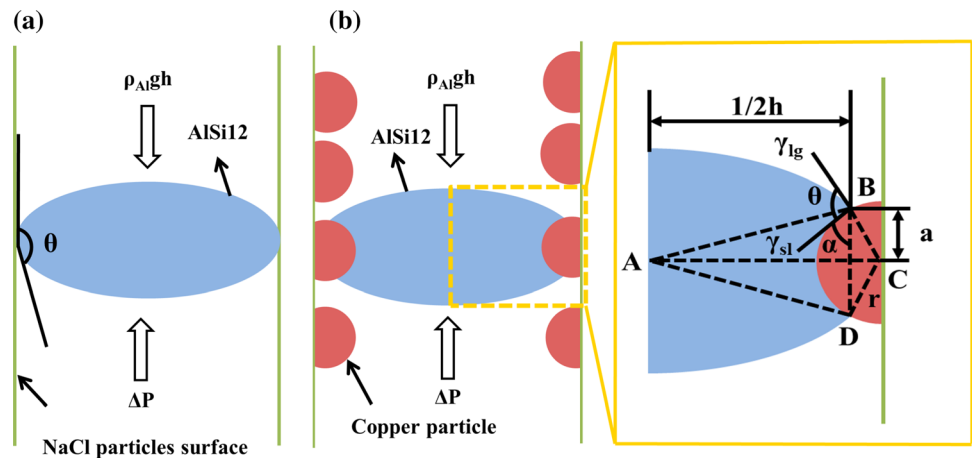


Figure 11 SEM images of the infiltrated AlSi12 alloy foam: **a** uncoated NaCl as preform and **b** copper-coated NaCl as preform.

Figure 12 Schematic diagram of AlSi12 alloy melt infiltration process to NaCl particles: **a** uncoated NaCl particles and **b** copper particles coated NaCl particles.



density of AlSi12 melt ($\rho = 2.65 \text{ g/cm}^3$), g is the gravitational acceleration coefficient ($g = 9.8 \text{ m/s}^2$), θ is the wetting angle, a is the contact radius ($a = 200 \text{ nm}$), α is the angle between the solid–liquid surface tension and the horizontal line of the liquid–gas–solid intersection equals $\arcsin(a/r)$. Finally, the calculated value of θ is 107° .

The wetting angle between AlSi12 alloy melt and the copper-coated NaCl particles is decreased, and the wettability is improved obviously.

Conclusion

In this paper, an innovative EC method was used to realize the uniform coating of copper crystals on the water-soluble NaCl particles. The affecting factors of copper coating effect, and the influence of copper-

plated NaCl particles on the pores structure of infiltrated AlSi12 foam were investigated and the following conclusions were drawn.

- 1 EC copper plating was achieved by the following steps: $\text{Cu}(\text{NO}_3)_2 \cdot 3\text{H}_2\text{O}$ was crystallized on NaCl particles by ethanol volatilization of the solution heated, and then thermally decomposed to obtain CuO coating which is finally reduced to Cu coating.
- 2 The pretreated NaCl particles increased the number of oxygen-containing functional groups, effectively enhanced the wettability of NaCl particles, appeared uniformly distributed thermal etch pits, which improved the bonding strength of the NaCl particles and $\text{Cu}(\text{NO}_3)_2 \cdot 3\text{H}_2\text{O}$ plating.
- 3 The addition of Tween-60 and PEG-6000 to the $\text{Cu}(\text{NO}_3)_2 \cdot 3\text{H}_2\text{O}$ solution inhibited the micro-

dissolution of NaCl particles in ethanol and promoted the formation of complete CuO coating which laid the foundation for achieving the complete Cu coating.

- 4 Infiltrated AlSi12 foam prepared from copper-plated NaCl particles has a more homogeneous pore structure and smaller pore size deviations than infiltrated AlSi12 foam obtained with uncoated NaCl particles, indicating that copper plating significantly improves the wettability of NaCl particles and AlSi12 alloy melt.

Acknowledgements

This work was funded by the National Natural Science Foundation of China Projects (52261009), and by the Key Research and Development Project of Yunnan Province, China (2018BA072, 2019ZE008). The authors would also express their appreciation to the Analytical and Testing Centre of Yunnan Province, P.R. China.

Author contributions

QX was contributed to software, formal analysis, data curation, writing—original draft, writing—review and editing. XZ was contributed to conceptualization, project administration, funding acquisition, writing—review and editing. JY was contributed to review and editing. YZ was contributed to review and editing. BH was contributed to review and editing.

Data availability

The data that support the findings of this study are available from the corresponding author upon reasonable request.

Declarations

Conflicts of interest We declare that we have no conflict of interest or personal relationships that could have appeared to influence the work reported in this paper.

Ethical approval No experiments involving human tissue were conducted in current study.

Supplementary information Not applicable.

References

- [1] Cao L, Fu Q, Si Y et al (2018) Porous materials for sound absorption. *Compos Commun* 10:25–35. <https://doi.org/10.1016/j.coco.2018.05.001>
- [2] Guiping C, Deping H, Guangji S (2001) Underwater sound absorption property of porous aluminum. *Colloids Surf A* 179:191–194. [https://doi.org/10.1016/S0927-7757\(00\)00656-7](https://doi.org/10.1016/S0927-7757(00)00656-7)
- [3] Banhart J (2006) Metal foams: production and stability. *Adv Eng Mater* 8:781–794. <https://doi.org/10.1002/adem.200600071>
- [4] Parveez B, Jamal NA, Maleque A et al (2021) Review on advances in porous Al composites and the possible way forward. *J Market Res* 14:2017–2038. <https://doi.org/10.1016/j.jmrt.2021.07.055>
- [5] Srinath G, Vadiraj A, Balachandran G et al (2010) Characteristics of aluminium metal foam for automotive applications. *Trans Indian Inst Met* 63:765–772. <https://doi.org/10.1007/s12666-010-0117-7>
- [6] Covaciu M, Walczak M, Ramos-Grez J (2011) A method for manufacturing cellular metals with open- and close-type porosities. *Mater Lett* 65:2947–2950. <https://doi.org/10.1016/j.matlet.2011.06.064>
- [7] Chang K, Gao J-T, Wang Z, Guo Z-C (2018) Manufacturing 3-D open-cell aluminum foam via infiltration casting in a super-gravity field. *J Mater Process Technol* 252:705–710. <https://doi.org/10.1016/j.jmatprotec.2017.10.032>
- [8] Kou DP, Li JR, Yu JL, Cheng HF (2008) Mechanical behavior of open-cell metallic foams with dual-size cellular structure. *Scr Mater* 59:483–486. <https://doi.org/10.1016/j.scriptamat.2008.04.022>
- [9] Wang H, Zhou X, Long B et al (2014) Thermal properties of open-celled aluminum foams prepared by two infiltration casting methods. *J Cent South Univ* 21:2567–2571. <https://doi.org/10.1007/s11771-014-2213-z>
- [10] Wan T, Liu Y, Zhou C et al (2021) Fabrication, properties, and applications of open-cell aluminum foams: a review. *J Mater Sci Technol* 62:11–24. <https://doi.org/10.1016/j.jmst.2020.05.039>
- [11] Cheng J, Gan X, Chen S et al (2019) Properties and microstructure of copper/nickel-iron-coated graphite composites prepared by electroless plating and spark plasma sintering. *Powder Technol* 343:705–713. <https://doi.org/10.1016/j.powtec.2018.11.057>
- [12] Liu Q, He X-B, Ren S-B et al (2014) Thermophysical properties and microstructure of graphite flake/copper

- composites processed by electroless copper coating. *J Alloy Compd* 587:255–259. <https://doi.org/10.1016/j.jallcom.2013.09.207>
- [13] Liu J, Zhang Y, Feng C et al (2019) Study of copper chemical-plating modified polyacrylonitrile-based carbon fiber wick applied to compact loop heat pipe. *Exp Thermal Fluid Sci* 100:104–113. <https://doi.org/10.1016/j.expthermflusci.2018.07.008>
- [14] Wang Y, Bian C, Jing X (2013) Adhesion improvement of electroless copper plating on phenolic resin matrix composite through a tin-free sensitization process. *Appl Surf Sci* 271:303–310. <https://doi.org/10.1016/j.apsusc.2013.01.188>
- [15] Ghaziof S, Gao W (2015) The effect of pulse electroplating on Zn–Ni alloy and Zn–Ni–Al₂O₃ composite coatings. *J Alloy Compd* 622:918–924. <https://doi.org/10.1016/j.jallcom.2014.11.025>
- [16] Han W, Qian X, Ma H et al (2021) Effect of nickel electroplating followed by a further copper electroplating on the micro-structure and mechanical properties of high modulus carbon fibers. *Mater Today Commun* 27:102345. <https://doi.org/10.1016/j.mtcomm.2021.102345>
- [17] Wan Y, Liu X, Hu X et al (2018) Effect of electroplating parameters on electroplated Cu film and microvoid formation of solder joints. *J Mater Sci Mater Electron* 29:18404–18416. <https://doi.org/10.1007/s10854-018-9955-6>
- [18] Gui C, Yao C, Huang J et al (2020) Preparation of polymer brush/Ni particle and its application in electroless copper plating on PA12 powder. *Appl Surf Sci* 506:144935. <https://doi.org/10.1016/j.apsusc.2019.144935>
- [19] Wang L, Xu L, Srinivasakannan C et al (2018) Electroless copper plating of tungsten powders and preparation of WCu₂₀ composites by microwave sintering. *J Alloy Compd* 764:177–185. <https://doi.org/10.1016/j.jallcom.2018.06.061>
- [20] Kelly PJ, Arnell RD (2000) Magnetron sputtering: a review of recent developments and applications. *Vacuum* 56:159–172. [https://doi.org/10.1016/S0042-207X\(99\)00189-X](https://doi.org/10.1016/S0042-207X(99)00189-X)
- [21] Tučkutė S, Urbonavičius M, Lelis M et al (2018) A new method of nanocrystalline nickel powder formation by magnetron sputtering on the water-soluble substrates. *Mater Res Express* 5:015017. <https://doi.org/10.1088/2053-1591/a0040>
- [22] Petukhov V, Bakin A, El-Shaer A-H et al (2007) Etch-pit density investigation on both polar faces of ZnO substrates. *Electrochim Solid State Lett* 10:H357. <https://doi.org/10.1149/1.2789285>
- [23] Patel AR, Bahl OP, Vagh AS (1966) Loops and spirals on thermally etched surfaces of cleaved NaCl crystals. *Jpn J Appl Phys* 5:870–873. <https://doi.org/10.1143/JJAP.5.870>
- [24] Koffyberg FP (1965) Etch pits and dislocations in SnO₂ crystals. *J Appl Phys* 36:844–849. <https://doi.org/10.1063/1.1714230>
- [25] Chang Y, Tao Y, Zhang Q, Yang Z-G (2015) Selective adsorption of catalyst and copper plating for additive fabrication of conductive patterns and through-holes. *Electrochim Acta* 158:7–12. <https://doi.org/10.1016/j.electacta.2015.01.161>
- [26] Huang J, Zhang Y, Yuan M et al (2019) A facile process to fabricate electroless plating on PET sheet: effects of surface roughness on adhesive force, electronic and structural properties of copper coating. *J Taiwan Inst Chem Eng* 97:406–413. <https://doi.org/10.1016/j.jtice.2019.01.018>
- [27] Wang Y, Wang Y, Chen J et al (2016) A facile process combined with inkjet printing, surface modification and electroless deposition to fabricate adhesion-enhanced copper patterns on flexible polymer substrates for functional flexible electronics. *Electrochim Acta* 218:24–31. <https://doi.org/10.1016/j.electacta.2016.08.143>
- [28] Liu W, Qiao X, Liu S et al (2019) A new process for pretreatment of electroless copper plating on the surface of mica powders with ultrasonic and nano-nickel. *J Alloy Compd* 791:613–620. <https://doi.org/10.1016/j.jallcom.2019.03.360>
- [29] Zhou X, Mao J, Qiao Z (2016) Electroless plating of copper layer on surfaces of urea–formaldehyde microcapsule particles containing paraffin for low infrared emissivity. *Particuology* 24:159–163. <https://doi.org/10.1016/j.partic.2014.12.006>
- [30] Ma Y, Guo L, Qi L et al (2021) Growth mechanism and thermal behavior of electroless Cu plating on short carbon fibers. *Surf Coat Technol* 419:127294. <https://doi.org/10.1016/j.surfcoat.2021.127294>
- [31] Kothekar SC, Ware AM, Waghmare JT, Momin SA (2007) Comparative analysis of the properties of Tween-20, Tween-60, Tween-80, Arlacel-60, and Arlacel-80. *J Dispersion Sci Technol* 28:477–484. <https://doi.org/10.1080/01932690601108045>
- [32] Li Z, Zhou Q (2010) PEG-6000 assisted growth of copper dendrites. *J Dispers Sci Technol* 31:1401–1404. <https://doi.org/10.1080/01932690903269545>
- [33] Ghose J, Kanungo A (1981) Studies on the thermal decomposition of Cu(NO₃)₂·3H₂O. *J Therm Anal* 20:459–462. <https://doi.org/10.1007/BF01912894>
- [34] Huang J, Tian C, Wang J et al (2018) Fabrication of selective electroless copper plating on PET sheet: effect of PET surface structure on resolution and adhesion of copper coating. *Appl Surf Sci* 458:734–742. <https://doi.org/10.1016/j.apsusc.2018.07.119>
- [35] Sun X, Wu D, Zhu W et al (2020) In-situ atomic-scale visualization of autocatalytic reduction of CuO with H₂.

Microsc Microanal 26:3048–3050. <https://doi.org/10.1017/S1431927620023648>

- [36] Liu B, Liu X, Liu M, Zhao Z (2011) Infiltration mechanism in SiCp/aluminum-matrix composite prepared by nonpressure. Mater Manuf Processes 26:1339–1345. <https://doi.org/10.1080/10426914.2010.537420>
- [37] An Q, Cong X, Shen P, Jiang Q (2019) Roles of alloying elements in wetting of SiC by Al. J Alloy Compd 784:1212–1220. <https://doi.org/10.1016/j.jallcom.2019.01.138>
- [38] Wu D, Wang P, Wu P et al (2015) Determination of contact angle of droplet on convex and concave spherical surfaces.

Chem Phys 457:63–69. <https://doi.org/10.1016/j.chemphys.2015.05.020>

Publisher's Note Springer Nature remains neutral with regard to jurisdictional claims in published maps and institutional affiliations.

Springer Nature or its licensor (e.g. a society or other partner) holds exclusive rights to this article under a publishing agreement with the author(s) or other rightsholder(s); author self-archiving of the accepted manuscript version of this article is solely governed by the terms of such publishing agreement and applicable law.